Pérez-López, S.; Fuster Escuder, JM.; Candelas Valiente, P.; Rubio Michavila, C. (2019). Fractal lenses based on Cantor binary sequences for ultrasound focusing applications. Ultrasonics. 99:105967-1-105967-6. https://doi.org/10.1016/j.ultras.2019.105967

Fractal lenses based on Cantor binary sequences for ultrasound focusing applications

Sergio Pérez-López[a], José Miguel Fuster[b], Pilar Candelas[a], Constanza Rubio[a]

[a] *Centro de Tecnologías Físicas, Universitat Politècnica de València, 46022, Spain*
[b] *Departamento de Comunicaciones, Universitat Politècnica de València, 46022, Spain*

Abstract

In this work, we demonstrate the application of Cantor fractal lenses in acoustics. The Cantor Zone Plate (CZP), previously introduced in optics, is designed from a conventional Fresnel Zone Plate (FZP) using a binary sequence governed by the distribution of a generalized Cantor set. The CZP maintains its main focus at the same focal distance than its associated FZP, providing a softer multi-foci focusing profile which is very useful in certain ultrasound therapeutic applications. Experimental measurements are in good agreement with the theoretical model, demonstrating that CZPs are suitable for the ultrasound field.

Keywords: Fractal, Cantor Set, Zone Plate, Ultrasound Focusing

1. Introduction

Wave focusing is a hot research topic in many areas of physics, such as optics [1], microwaves [2], X-rays [3] or acoustics [4, 5]. Among the different types of lenses with focusing capabilities, Fresnel Zone Plates (FZPs) stand out for their easier fabrication process compared with traditional curved lenses. FZPs consist on a set of concentric rings, being each one of them a Fresnel region. The width of each ring depends on parameters such as the focal distance and the wavelength. There are two different types of zone plates (ZPs) depending on how the Fresnel regions are implemented. Soret

Email address: serpelo1@teleco.upv.es (Sergio Pérez-López)

ZPs [6] alternate transparent with opaque regions, while Rayleigh-Wood ZPs [7, 8] replace opaque areas with phase-reversal regions.

In the last years, new types of lenses based on the use of binary sequences have been proposed in optics, such as Fibonacci ZPs [9, 10], Cantor ZPs [11, 12, 13] and Thue-Morse ZPs [14, 15]. All these novel ZPs are variations over conventional FZPs, where transparent and opaque/phase-reversal Fresnel regions are distributed according to a specific binary sequence. Cantor ZPs (CZPs) are based on binary sequences that are governed by a fractal structure known as the generalized Cantor set, and they present a multifocal focusing profile with interesting self-similar properties. They become appealing alternatives in therapeutic applications [16, 17, 18, 19] where a softer tissue heating profile is desired.

Although alternative approaches in Cantor planar lenses design have been previously reported in ultrasounds [20, 21], these designs are not based on FZPs and do not allow to control the zone plate focusing profile features. As an example, the location of the lens main focus is an unknown at the design stage and cannot be determined until these type of lenses are fully characterized after fabrication. However, with the design method that provided in this work, we can accurately establish the location of the main focus at the design stage as in the conventional FZP case.

As it has been previously addressed in [22], the decision of whether selecting a transparent or an opaque central region in a FZP is a design parameter that becomes critical when directional transducers are employed. In this work, we show that this parameter also plays a significant role in the focusing enhancement of CZPs.

2. Theory

As stated previously, CZPs are based on conventional FZPs, although a CZP uses a different criterion based on its governing binary sequence to determine whether a certain Fresnel region is either transparent or opaque/phase-reversal. In our setup, the distance between the transducer and the lens is not long enough to consider plane wave incidence, and therefore, the radii of the different Fresnel regions are calculated considering the spherical wave incidence equation:

$$d + F + \frac{n\lambda}{2} = \sqrt{r_n^2 + F^2} + \sqrt{r_n^2 + d^2}, \tag{1}$$

where F represents the focal distance, d is the separation between the lens and the transducer, λ is the wavelength, r_n is the n-th Fresnel radius and $n = 1, 2, ..., N$, being N the total number of Fresnel regions.

Once the different Fresnel radii have been calculated, the Fresnel regions are established. Then, different types of ZPs can be generated by stating which of the Fresnel regions become transparent areas or opaque/phase-reversal areas, using a binary sequence to provide this information. The binary sequence length is equal to the total number of Fresnel regions, and each position in the binary sequence maps to its corresponding Fresnel region. In Soret ZPs, type-1 and type-0 elements of the binary sequence represent opaque and transparent regions, respectively, or vice versa. We define a O-ZP ("O-" stands for opaque) when type-1 elements represent opaque sections, while a T-ZP ("T-" stands for transparent) relates type-1 elements with transparent regions. Hence, O-ZPs present an opaque central region, while their T-ZPs counterparts present a transparent central region.

For instance, a periodic binary sequence of N elements of alternating "1"s and "0"s produces a conventional FZP of N Fresnel regions as shown in Figures 1(a), 1(b) and 1(c). In this case an O-FZP has been implemented, as type-1 elements represent opaque regions.

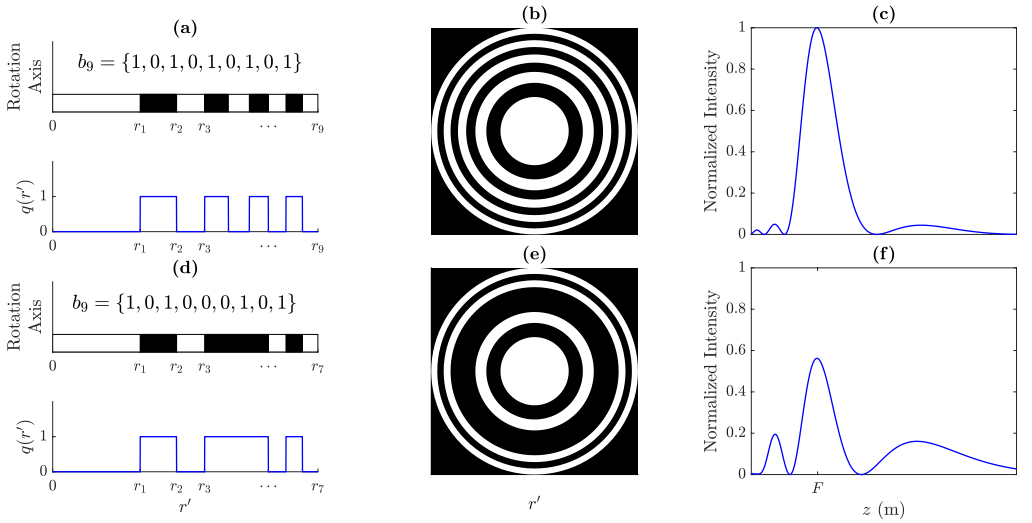

Figure 1: FZP design example with $N = 9$: (a) Periodic binary sequence and its corresponding pupil function, (b) FZP layout and (c) FZP focusing profile. CZP design example with $N = 9$: (d) Generalized Cantor sequence with $M = 2$ and $S = 2$ and its corresponding pupil function, (e) CZP layout, (f) CZP focusing profile.

In order to generate a Cantor binary sequence, an initial sequence of $2M-1$ elements, known as the generator, is created at the first stage ($S=1$), with M type-1 elements and $M-1$ type-0 elements, sorted with an alternating distribution. On the next stages, type-1 elements are replaced with replicas of the generator sequence, while each type-0 element is replaced with a sequence of "0"s of the same length as the generator. The number of elements in the Cantor binary sequence at any stage can be calculated as $N=(2M-1)^S$. Table 1 shows several examples of Cantor binary sequences for different values of M and S, while table 2 shows a comparison between the binary sequences of three CZPs with $N=9$, $N=25$ and $N=27$ elements and their associated binary sequences of conventional FZPs with the same number of regions. The associated FZP is always a periodic binary sequence of the same length than the original Cantor binary sequence.

M	S	Cantor binary sequence	N
2	1	{101}	3
	2	{101000101}	9
	3	{101000101000000000101000101}	27
3	1	{10101}	5
	2	{1010100000101010000010101}	25
4	1	{1010101}	7

Table 1: Cantor binary sequences for different combinations of M and S.

N	Zone Plate	Binary sequence
9	CZP	{101000101}
	FZP	{101010101}
25	CZP	{1010100000101010000010101}
	FZP	{1010101010101010101010101}
27	CZP	{101000101000000000101000101}
	FZP	{1010101010101010101010101}

Table 2: Binary sequences for different CZPs and their associated FZPs.

Hence, once the different Fresnel regions of the conventional FZP are generated using equation 1, the Cantor binary sequence defines the lens pupil function which is used to generate the CZP, as it can be observed in Figure 1(d), 1(e) and 1(f). The pupil function, $q(r')$, describes the geometry of the

lens, indicating whether a specific Fresnel region is transparent or opaque to the ultrasound emission. In O-ZPs, type-1 elements correspond to $q(r') = 0$ (opaque regions), while type-0 elements determine $q(r') = 1$ (transparent regions). On the contrary, in T-ZPs, type-1 and type-0 elements correspond to $q(r') = 1$ (transparent) and $q(r') = 0$ (opaque), respectively. Thus, both the FZP and the CZP shown in Figure 1 correspond to O-ZPs. As it can be observed from Figures 1(c) and 1(f), the distribution of the acoustic intensity along the focusing profile is different for FZPs and CZPs. While a FZP concentrates the acoustic intensity at a single focal point, the CZP distributes its focusing profile among three different foci, a main focus at the same location than that of the associated FZP, and two additional foci with lower intensities that soften the overall focusing profile and can be very appealing in certain therapeutic applications. Thus, the acoustic intensity is distributed differently in both focusing profiles.

To analyze the focusing properties of a CZP, or in general of any ZP, the acoustic intensity generated by the lens can be numerically calculated using the Rayleigh-Sommerfeld diffraction integral [23]:

$$I(r,z) = \frac{1}{2\rho_0 c_0 \lambda^2} \left| \int_0^{2\pi} \int_0^{+\infty} q(r') p_i(r') \frac{r'}{R} \cos(n,R) e^{-jkR} dr' d\varphi \right|^2, \quad (2)$$

where $k = 2\pi/\lambda$ is the wavenumber, r is the radial axis, z is the longitudinal axis, r' is the radial axis at the surface of the lens, φ is the rotation angle at the surface of the lens, $p_i(r')$ is the incident pressure at the lens, $q(r')$ is the pupil function, $R = \sqrt{z^2 + r^2 + (r')^2 - 2rr'\cos\varphi}$ and $\cos(n,R) = z/R$, being n the normal direction to the lens surface. ρ_0 and c_0 are the density and sound speed of the host medium, respectively, which in this case is water.

In the plane wave incidence case, $p_i(r')$ is constant and does not affect the integral result. However, in the ultrasound case, a piston transducer is employed as an emitter, affecting the lens focusing profile [22]. In the far field, the piston transducer can be modelled as a point source emitter with a given directivity pattern:

$$p_i(r') = \frac{jkp_0a^2}{2\sqrt{(r')^2 + d^2}} D(r') e^{-jk\sqrt{(r')^2+d^2}}, \quad (3)$$

with a being the piston active radius, p_0 the pressure at the surface of the

piston and $D(r')$ the piston directivity pattern, which is given by

$$D(r') = \frac{2J_1(ka\sin\theta)}{ka\sin\theta}, \tag{4}$$

where J_1 is the first kind and first order Bessel function and $\theta = \arctan(r'/d)$ is the angle referred to the normal direction of the surface of the piston.

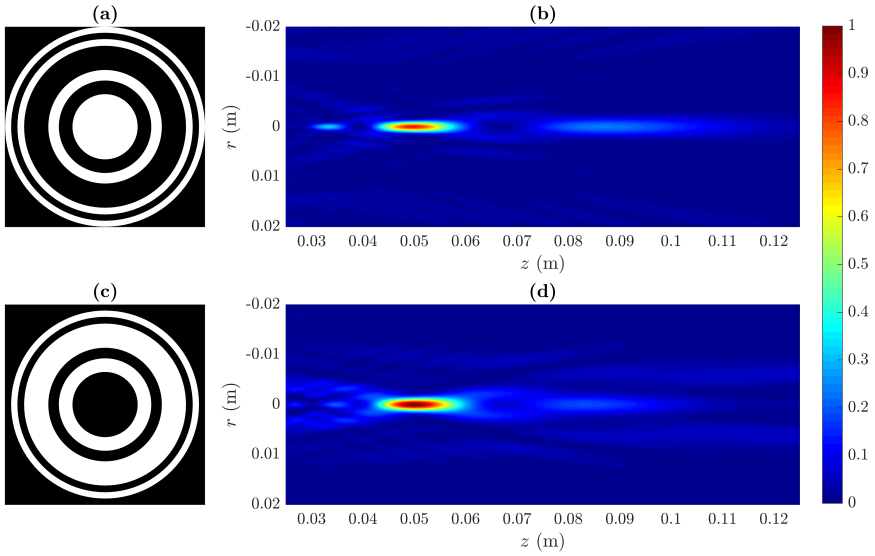

Figure 2: Numerical results: (a) O-CZP and (b) its computed intensity map, (c) T-CZP and (d) its computed intensity map.

Figure 2 shows simulated normalized intensity maps for two different CZPs. Intensity maps have been computed using equation 2, considering a piston transducer with 12.7 mm of active diameter. Both CZPs are obtained for $M = 2$ and $S = 2$, a focal distance of $F = 50$ mm, a working frequency of 1 MHz and a transducer separation distance of $d = 340$ mm. The difference between both CZPs is that the first one has been designed considering a central pressure blocking region (O-CZP) while the second one has been designed considering a central transparent region (T-CZP). As it can be observed from Figures 2(b) and 2(d), the T-CZP (Figure 2(c)) achieves a higher intensity level at the focal distance compared to the O-CZP (Figure 2(a)). This phenomenon is a consequence of the directional behaviour of the piston transducer, as its main energy contribution is generated at the perpendicular direction of the transducer surface. Thus, in the O-CZP case, the main

energy contribution is reflected back at the central blocking region, whereas in the T-CZP case, it fully contributes to the focal intensity, enhancing the CZP focusing capability. Both CZP intensity maps have been normalized to the maximum value for comparison purposes, which corresponds to the T-CZP case.

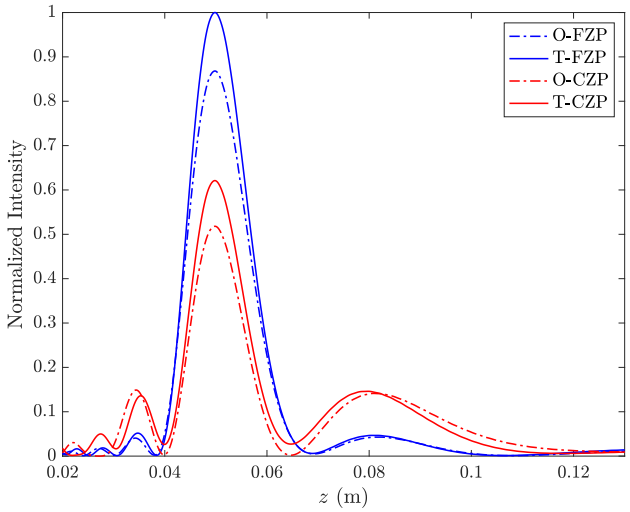

Figure 3: Focusing profiles for O-CZP (red dashed line), T-CZP (red solid line) and their associated O-FZP (blue dashed line) and T-FZP (blue solid line). In all cases, $F = 50$ mm, $d = 340$ mm and $\lambda = 1.5$ mm.

Figure 3 depicts the focusing profiles of the acoustic intensity maps shown in Figure 2 compared to the focusing profiles of their associated FZPs with the same focal distance and for both transparent (T-) and opaque (O-) central regions. All focusing profiles have been normalized to the maximum intensity value, which corresponds to the T-FZP case. As it can be observed from Figure 3, both FZP lenses achieve higher focal intensities than their corresponding CZPs, because CZPs distribute the incident energy among their secondary foci. Moreover, Figure 3 also shows that lenses with transparent central regions (T-FZP and T-CZP) achieve a higher focal intensity than their associated counterparts with opaque central regions (O-FZP and O-CZP), as a consequence of the directional ultrasound emission of the transducer. However, it is worth noting that although the T-CZP reaches a higher intensity value than the O-CZP, the T-CZP presents a more distorted focusing profile. This distortion translates into a small focal displacement and

intensity reduction of the secondary foci, which are slightly shifted towards the main focus and provide lower relative intensity levels when compared to the O-CZP focusing profile. Although this distortion is very low, there is a trade-off between focal intensity level and focusing profile distortion when selecting T-CZPs over O-CZPs.

3. Experimental Results

Experimental measurements have been carried out to demonstrate that CZPs are suitable for ultrasound focusing applications. Figure 4 shows the experimental set-up, which consists of a 3D underwater automated positioning system with a spatial resolution of $1 \times 1 \times 1$ mm^3 and three degrees of freedom. The signal is generated using a Panametrics 5077PR pulser and then, it is transmitted using a piston transducer from Imasonic with a 12.7 mm active diameter and a central frequency of 1 MHz. A needle hydrophone from Precision Acoustics with a diameter of 1.5 mm is used as receiver, and its output signal is amplified using a low noise preamplifier and then digitized, using a digital oscilloscope from Pico Technology.

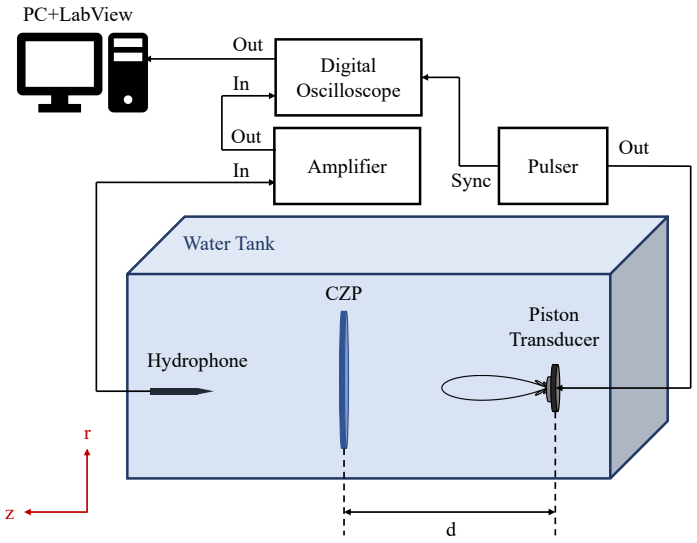

Figure 4: Schematic view of the experimental set-up.

Two Soret CZPs have been manufactured using brass for implementing the opaque Fresnel regions, because this material presents a high acoustic

impedance contrast with water. Both CZPs have been designed with $M = 2$ and $S = 2$ for an operating frequency of 1 MHz ($\lambda = 1.5$ mm), a focal distance $F = 50$ mm and a separation between the lens and the transducer of $d = 340$ mm. Figure 5(a) shows a O-CZP (blocking central region), whereas Figure 5(c) shows a T-CZP (transparent central region). The outermost radius of the O-CZP is $r_N = 24.87$ mm, whereas for the T-CZP is $r_N = 23.38$ mm. Thus, the T-CZP presents a smaller size compared to the O-CZP because the O-CZP implements one additional Fresnel opaque region. Figures 5(b) and 5(d) show the corresponding measured intensity maps. Both measured intensity maps are normalized to the higher value, which corresponds to the T-CZP case, following the same procedure as previously in the simulation. As it can be observed from Figure 5, T-CZP achieves a higher focal intensity level than O-CZP, which agrees with numerical results shown in Figure 2.

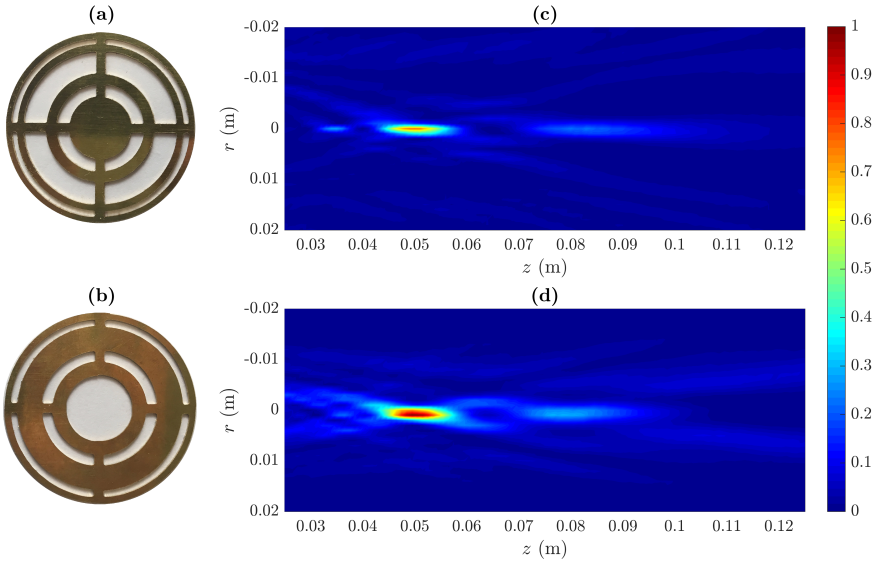

Figure 5: Experimental results: (a) O-CZP and (b) its measured intensity map, (c) T-CZP and (d) its measured intensity map.

Figure 6 shows the longitudinal and transversal cuts corresponding to both O-CZP and T-CZP. Blue solid lines represent experimental results, while red dashed lines correspond to numerical results. Figures 6(a) and 6(b) depict axial longitudinal cuts, also known as focusing profiles, against the axial coordinate. The results show good agreement between simulations and experimental measurements. The triple-foci focusing profile, which cor-

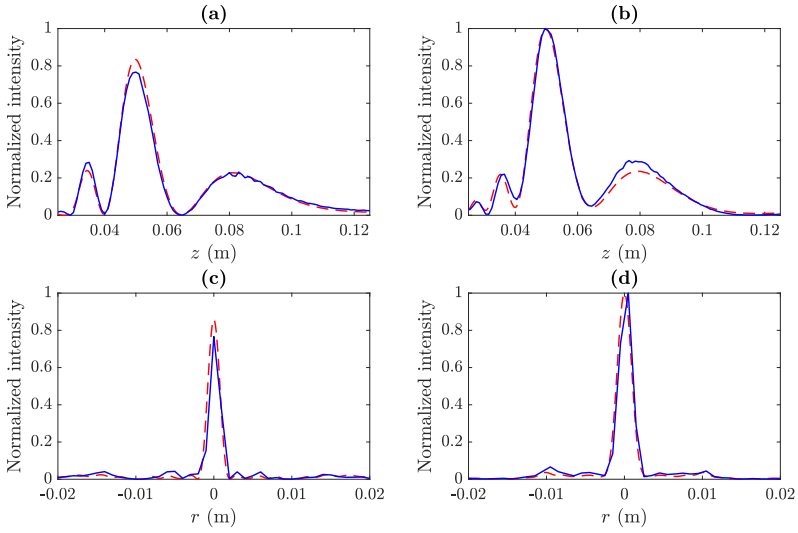

Figure 6: O-CZP: (a) focusing profile and (c) transversal cut at the focal plane. T-CZP: (b) focusing profile and (d) transversal cut at the focal plane. Blue solid lines represent experimental measurements and red dashed lines correspond to numerical results.

responds to $M = 2$ and $S = 2$, has potential applications in therapeutic treatments where a softer progressive heating profile is required. Experimental measurements and simulation results match very well at the main lobe of both lenses, which present Full Length Half Maximum (FLHM) values of 11.48 mm for O-CZP and 11.39 mm for T-CZP (Table 3), being both foci located at the designed focal length of 50 mm. The secondary foci of the O-CZP are located at 35 and 81 mm, while the secondary foci of the T-CZP are located closer to the main focus at 36 and 77 mm, which agrees with the results depicted in Figure 3. However, slight differences between simulations and experiments can be appreciated at the focusing profile secondary lobes. These small differences are mainly due to the cross-shaped mechanical support of the manufactured CZPs that can be observed in Figures 5(a) and 5(c), which maintain the FZP brass rings fixed in place. This cross-shaped structure has not been considered in the simulation. Figures 6(c) and 6(d) depict transversal the cuts at the focal distance against the radial coordinate for O-CZP and T-CZP, respectively. Both simulation and experimental results agree again very well, showing transversal profiles with negligible side lobes and with a narrow main lobe which presents Full Width Half Maxi-

mum (FWHM) values of 1.59 mm in the O-CZP case and 2.09 mm in the T-CZP case, as shown in Table 3. This absence of secondary lobes in the transversal cuts is due to the piston transducer influence, as the amplitude of the incident pressure at the lens in this case has a similar effect to FZP apodization through decreasing diffraction efficiency regions [24].

Table 3 shows, as stated before, the measured FLHM and FWHM for both CZP lenses, but it also provides the measured normalized intensity at the focus, which becomes a very significant parameter, and demonstrates that when operating in underwater ultrasound with piston emitters, the choice of whether the central Fresnel region is transparent or opaque is critical [22]. The T-CZP option (transparent central Fresnel region) results in a 30.43% enhancement at the focal point intensity over the O-CZP option (opaque central Fresnel region). This significant improvement in the focusing capabilities of the CZP lens is due to the use of directional piston transducers, which favors the use of central transparent regions.

	F (mm)	FLHM (mm)	FWHM (mm)	I_F
O-CZP	50	11.48	1.59	76.67%
T-CZP	50	11.39	2.09	100%

Table 3: Measured F, FLHM, FWHM and normalized focal intensity (I_F) values for O-CZP and T-CZP.

Figure 7 depicts the focusing profiles of the manufactured CZPs at three different frequencies: $f = 0.9$ MHz (blue lines), $f = 1.0$ MHz (black lines), which corresponds to the design frequency, and $f = 1.1$ MHz (red lines). Figures 7(a) and 7(b) correspond to the O-CZP and T-CZP cases, respectively. Numerical results are depicted with dashed lines, whereas experimental measurements are depicted with solid lines. As it can be observed from figure 7, the modification of the operating frequency shifts the lens focal distance. Both O-CZP and T-CZP shift their focal distance to $F = 56.35$ mm when the operating frequency is increased to $f = 1.1$ MHz. In contrast, when the frequency is reduced to $f = 0.9$ MHz, the focal distance is shifted to $F = 43.46$ mm. Moreover, the secondary foci of the CZP profile are also shifted similarly with the operating frequency. Figure 7 illustrates that the magnitude of the shift is related to the current focal length. Thus, the secondary focus that is farther from the lens is the focus that presents a higher shift when the operating frequency is modified. Hence, the operating frequency becomes an additional parameter very appealing to dynamically control the

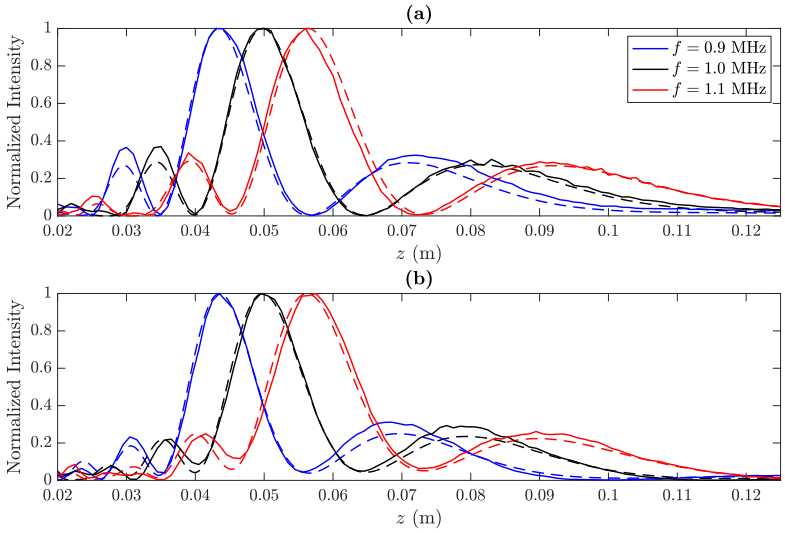

Figure 7: Focusing profile for manufactured CZPs at different frequencies: (a) O-CZP and (b) T-CZP. All profiles are normalized to their maximum values. Solid lines represent experimental measurements, while dashed lines represent numerical results.

focal distance of CZP lenses.

4. Conclusion

In this work, theoretical analysis on the design and experimental characterization of Cantor Zone Plates have been carried out. These lenses produce focusing profiles with their main focus at the same location than their associated FZPs and multiple secondary lobes. Experimental results for two manufactured CZPs have been presented, showing good agreement with the theoretical model. Results show that when using directional piston emitters in underwater transmission, CZPs designed with central transparent regions (T-CZPs) achieve higher focal intensity levels than those designed with central pressure blocking regions (O-CZPs). It has been experimentally demonstrated that the measured focal intensity of the T-CZP case provides a 30.43% enhancement of the intensity level compared to the O-CZP case. Thus, this work shows that CZPs become appealing alternatives in ultrasound focusing applications, such as therapeutic treatments which require a softer heating profile.

Acknowledgments

This work has been supported by Spanish MINECO (TEC2015-70939-R), MICINN (RTI2018-100792-B-I00) and by Universitat Politècnica de València research grant program PAID-01-18.

References

[1] R. S. Rodrigues Ribeiro, P. Dahal, A. Guerreiro, P. A. S. Jorge, J. Viegas, Fabrication of Fresnel plates on optical fibres by FIB milling for optical trapping, manipulation and detection of single cells, Scientific Reports 7 (2017) 4485.

[2] H. Hristov, M. Herben, Millimeter-wave Fresnel-zone plate lens and antenna, IEEE Transactions on Microwave Theory and Techniques 43 (1995) 2779–2785.

[3] K. Jefimovs, O. Bunk, F. Pfeiffer, D. Grolimund, J. van der Veen, C. David, Fabrication of Fresnel zone plates for hard X-rays, Microelectronic Engineering 84 (2007) 1467–1470.

[4] D. C. Calvo, A. L. Thangawng, M. Nicholas, C. N. Layman, Thin Fresnel zone plate lenses for focusing underwater sound, Applied Physics Letters 107 (2015) 014103.

[5] J. M. Fuster, P. Candelas, S. Castiñeira-Ibáñez, S. Pérez-López, C. Rubio, Analysis of fresnel zone plates focusing dependence on operating frequency, Sensors (Switzerland) 17 (2017) 2809.

[6] J. L. Soret, Ueber die durch Kreisgitter erzeugten Diffractionsphänomene, Annalen der Physik und Chemie 232 (1875) 99–113.

[7] L. Rayleigh, Wave Theory, volume 24, 1888.

[8] J. Kirz, Phase zone plates for x rays and the extreme uv, Journal of the Optical Society of America 64 (1974) 301.

[9] J. A. Monsoriu, A. Calatayud, L. Remon, W. D. Furlan, G. Saavedra, P. Andres, Bifocal Fibonacci Diffractive Lenses, IEEE Photonics Journal 5 (2013) 3400106–3400106.

[10] F. Machado, V. Ferrando, W. D. Furlan, J. A. Monsoriu, Diffractive m-bonacci lenses, Optics Express 25 (2017) 8267.

[11] G. Saavedra, W. D. Furlan, J. A. Monsoriu, Fractal zone plates, Optics Letters 28 (2003) 971.

[12] W. D. Furlan, G. Saavedra, J. A. Monsoriu, White-light imaging with fractal zone plates, Optics Letters 32 (2007) 2109.

[13] O. Mendoza-Yero, M. Fernández-Alonso, G. Mínguez-Vega, J. Lancis, V. Climent, J. A. Monsoriu, Fractal generalized zone plates, Journal of the Optical Society of America A 26 (2009) 1161.

[14] V. Ferrando, F. Giménez, W. D. Furlan, J. A. Monsoriu, Bifractal focusing and imaging properties of Thue–Morse Zone Plates, Optics Express 23 (2015) 19846.

[15] T. Xia, S. Cheng, S. Tao, Generation of three equal-intensity foci based on a modified composite zone plate, Optik 159 (2018) 150–156.

[16] G. ter Haar, C. Coussios, High intensity focused ultrasound: Physical principles and devices, International Journal of Hyperthermia 23 (2007) 89–104.

[17] D. Suo, Z. Jin, X. Jiang, P. A. Dayton, Y. Jing, Microbubble mediated dual-frequency high intensity focused ultrasound thrombolysis: An In vitro study, Applied Physics Letters 110 (2017) 023703.

[18] S. GyP, L. DY, H. G, What is on the Horizon for Hyperthermic Cancer Therapy?, Journal of Traditional Medicine & Clinical Naturopathy 06 (2017).

[19] J. C. Simon, O. A. Sapozhnikov, V. A. Khokhlova, Y.-N. Wang, L. A. Crum, M. R. Bailey, Ultrasonic atomization of tissue and its role in tissue fractionation by high intensity focused ultrasound, Physics in Medicine and Biology 57 (2012) 8061–8078.

[20] S. Castiñeira-Ibáñez, D. Tarrazó-Serrano, J. Fuster, P. Candelas, C. Rubio, Polyadic Cantor Fractal Ultrasonic Lenses: Design and Characterization, Applied Sciences 8 (2018) 1389.

[21] D. Tarrazó-Serrano, S. Castiñeira-Ibáñez, P. Candelas, J. M. Fuster, C. Rubio, Numerical simulation and laboratory measurements on the influence of fractal dimension on the acoustic beam modulation of a Polyadic Cantor Fractal lenses, Applied Acoustics 148 (2019) 119–122.

[22] S. Pérez-López, J. M. Fuster, P. Candelas, C. Rubio, On the focusing enhancement of Soret zone plates with ultrasound directional transducers, Applied Physics Letters 114 (2019) 224101.

[23] J. W. Goodman, Introduction to Fourier optics, Roberts and Company Publishers, 2005.

[24] A. Takeuchi, K. Uesugi, Y. Suzuki, Improvement of quantitative performance of imaging x-ray microscope by reduction of edge-enhancement effect, Journal of Physics: Conference Series 849 (2017) 012055.